Journal of Electroanalytical Chemistry, 375 (1994) 141–155

Dynamics of surface alloying promoted by cadmium underpotential deposition–anodic stripping cycles on irregular silver electrodeposits

M.E. Martins, A. Hernández-Creus *, R.C. Salvarezza, and A.J. Arvia **

Instituto de Investigaciones Fisicoquímicas Teóricas y Aplicadas (INIFTA), Universidad Nacional de La Plata, Sucursal 4, Casilla de Correo 16, (1900) La Plata (Argentina)

(Received 16 November 1993; in revised form 17 February 1994)

Abstract

The underpotential deposition of Cd from dilute aqueous 5×10^{-3} M $CdSO_4$ + 0.5 M Na_2SO_4 + 0.01 M H_2SO_4 on Ag electrodeposits grown on polyfaceted Pt single-crystal microspheres was studied using potentiodynamic and potentiostatic techniques, transmission electron diffraction, scanning tunneling microscopy and X-ray photoelectron spectroscopy.

Ag electrodeposits were grown in 5×10^{-3} M Ag_2SO_4 + 0.5 M Na_2SO_4 + 0.01 M H_2SO_4 at cathodic overpotentials η_c of −0.06 V and −0.58 V to form a columnar and dendritic Ag surface respectively.

Surface rearrangement processes involving the formation of Cd + Ag alloys were studied by stripping voltammetry after the potential was held for a certain time at different preset values covering the potential range in which the degree of surface coverage by Cd atoms was less than or close to unity ($\theta_c \leq 1$) on both Ag surfaces. Surface diffusion and penetration of Cd atoms into bulk Ag for $\theta_c \leq 1$ are discussed. A place-exchange mechanism is advanced to account for the kinetics of Cd + Ag alloy formation.

1. Introduction

The early stages of metal phase growth of an epitaxial film imply the formation of an interfacial region which can be described by different models involving a discontinuous monolayer, a transition monolayer or a diffusive interface [1,2]. The diffusive interface is related to the formation of either a solid solution or an ordered alloy. In this case, lattice misfit and surface alloying can make the modelling of experimental data rather difficult.

Metal underpotential deposition (UPD) on foreign substrates can be considered as a condensation of metal atoms through adsorption or nucleation which precedes metal phase growth. Over the last few decades metal UPD on well-defined surfaces has become an important area of electrochemistry because results from these studies have provided the opportunity to explore possible links between electrochemical and gas phase reactions at metal surfaces. This matter has been extensively reviewed in several publications [3–5].

According to thermodynamics, alloy formation is possible even in the UPD potential range in those systems forming stable intermetallic phases or exhibiting sufficient miscibility between substrate and adsorbate metals. This behavior has been observed in a number of polycrystalline [6–8] and single-crystal [9–16] substrates. Alloying in the UPD potential range can be explained by a place-exchange mechanism involving surface atoms and vacancies leading to dermalloying formation. Dermalloying kinetics differs, in principle, from the kinetics of metal penetration into the bulk substrate. Dermalloying kinetics at a grain-boundary-free metal surface is usually determined by the surface diffusion rate of the slowest moving particles.

The electrocatalytic properties of dermalloys are still a matter of fundamental research. Their application in electrocatalysis depends on the possibility of producing dermalloyed electrodes, large surface area, for instance, by using very irregular dermalloyed fully accessible substrates. A large surface area of either columnar or dendritic electrodeposits can easily be produced at intermediate and high growth rates re-

* Visiting Professor, Departamento de Química Física, Universidad de La Laguna, Tenerife, Spain.

** To whom correspondence should be addressed.

0022-0728/94/$7.00
SSDI 0022-0728(94)03395-J

spectively [17,18]. Such electrodeposits have recently been considered as reference systems for describing irregular surface growth patterns predicted by theoretical models [19]. These two types of metallic electrodeposits exhibit a clear growth transition from a columnar to a dendritic pattern as the applied potential is moved in the direction of increasing the metal electrodeposition rate. Columnar and dendritic metal surfaces appear as suitable large surface area substrates for attempting dermalloy formation [17,18].

This work is devoted to dermalloying and bulk alloy formation from Cd electrodeposition on irregular Ag substrates electrodeposited on polycrystalline Pt surfaces. Previous investigations related to this subject have shown that Cd UPD on Ag at potentials close to the Cd/Cd^{2+} reversible electrode potential implies the formation of several Cd monolayers. The binary Cd + Ag system forms intermetallic phases [20], and Cd + Ag alloys are thermodynamically stable in the Cd UPD potential range on Ag [9,10].

Two main aspects are considered in this work, namely substrate characterization by transmission electron diffraction (TED), scanning tunneling microscopy (STM) and different UPD reactions, and investigation of the Cd + Ag dermalloy kinetics in aqueous acid solutions using electrochemical methods and X-ray photoelectron spectroscopy (XPS). Cd UPD at both rough columnar and dendritic Ag surfaces produces Cd + Ag dermalloy films up to two monolayers (2 ML) thick for degrees of surface coverage by Cd atoms lower than unity ($\theta_c \leq 1$). Dermalloy kinetics appear to be determined by the mobility of Ag surface atoms into a mobile Cd surface layer.

2. Experimental

2.1. Electrode preparation

Two types of Ag working electrodes (WEs), which were characterized by either a columnar or a dendritic topography, were used. In both cases, the Ag electrodeposits were grown on either a polyfaceted Pt single-crystal microsphere (apparent area 0.027 cm^2) or a polycrystalline Pt plate (apparent area 2 cm^2). Ag-plated Pt plate electrodes were specifically used for Auger and XPS analyses.

Ag electrodeposits were made from a 0.5 M Na_2SO_4 + 10^{-2} M H_2SO_4 + 5×10^{-3} M Ag_2SO_4 solution (solution I) under constant-potential conditions. Depending on the applied cathodic overvoltage η_c, either a compact columnar ($\eta_c = -0.06$ V) [17] or a rough dendritic ($\eta_c = -0.58$ V) [18] Ag electrodeposit was formed. The cathodic overpotential is defined as $\eta_c = E_r - E_d$, where E_r is the reversible potential of the Ag/Ag^+ couple in solution I and E_d is the applied potential ($E_r = 0.38$ V/SCE at 25°C) [21]. Potentials in the text are referred to the saturated calomel electrode (SCE) scale. The value of the Ag electrodeposition charge density q_{Ag} was varied in the range 25 mC $cm^{-2} < q_{Ag} < 60$ mC cm^{-2}. After preparation, the Ag-coated WE was removed from the cell at E_d, rinsed with Milli-Q* water and transferred to another electrochemical cell containing 0.5 M $Na_2SO_4 + 10^{-2}$ M $H_2SO_4 + 5 \times 10^{-3}$ M $CdSO_4$ (solution II). The reversible potential of the Cd/Cd^{2+} couple in solution II is $E_r = -0.71$ V/SCE at 25°C [21]. The potential was then stepped to $E_h = 0.15$ V, i.e. a potential sufficiently negative to prevent oxidation of the Ag electrodeposit but positive enough to avoid Cd UPD on Ag.

The Cd + Ag alloy (α phase) electrodes were prepared by melting known amounts of Ag and Cd in a quartz tube under vacuum [22]. For this preparation, small-size high purity Ag and Cd grains were employed. Each lens-shaped alloy piece resulting from melting was machined to make square plate electrodes of apparent area about 1 cm^2, with a metal stripe on one side to facilitate welding to a Pt lead. The Cd + Ag alloy electrode was then mirror polished with alumina suspension of 1.0 and 0.3 μm grit alumina in ethanol.

2.2. Electrochemical measurements

Electrochemical measurements were made in a conventional three-electrode glass cell comprising a WE, a large Pt gauze counter-electrode and a saturated calomel reference electrode conventionally assembled. Solutions were prepared from Merck p.a. chemicals and Milli-Q* water, and were kept under purified N_2. Runs were made at 25°C under a N_2 atmosphere.

Changes of Ag electrodeposits were followed by Cd UPD–anodic stripping cyclic voltammetry at 0.02 V s^{-1} between E_{sc} and E_{sa}, the lower and upper switching potentials respectively. The value of $E_{sc} = -0.585$ V was used in most of the runs to approach the $\theta_c \leq 1$ condition for Cd atom coverage.

After the first cyclic voltammogram (CV 1) had been recorded, the potential was scanned downwards from 0.15 V to E_h (-0.585 V $< E_h < 0.15$ V), and then held at E_h for a preset time t_h (60 s $< t_h <$ 30 h). Subsequently, the cyclic voltammogram was continued to obtain the second anodic stripping voltammogram (CV 2) and so on. The comparison between CV 1 and CV 2 allowed us to infer possible rearrangements at the Ag surface produced by potential holding at E_h in the time t_h. Finally, in all cases the potential cycling was continued until the initial stable voltammogram was recovered.

Cd UPD–anodic stripping voltammetry was also run on Cd + Ag alloy WE, with the intention of correlating

the voltammetric features found for these electrodes with those resulting from Cd UPD on Ag electrodes under certain operating conditions. Differences could be assigned to formation of a Cd + Ag alloy.

2.3. Surface area determination

The real surface area of Pt substrates was measured by the H atom electrosorption voltammetric charge in 0.5 M H_2SO_4 at 0.1 V s^{-1}, covering the −0.21 V to 1.23 V range. For this purpose, the charge density q_M of the H adatom monolayer (ML) on Pt was taken as 0.21 mC cm^{-2}. Otherwise, the surface area of Ag electrodeposits was evaluated from the Cd UPD–anodic stripping charge of CV 1 between 0.15 V and −0.585 V, taking $q_M = 0.42$ mC cm^{-2} for the Cd ML.

2.4. Surface characterization

Surface characterization was based upon Pb UPD, TED and STM data.

2.4.1. Pb underpotential deposition

Columnar and dendritic Ag surfaces were characterized by Pb UPD–anodic stripping cyclic voltammetry in 0.1 M $NaClO_4$ + 5 × 10^{-3} M $HClO_4$ + 10^{-2} M $Pb(ClO_4)_2$ at 0.01 V s^{-1} in the 0 V to −0.43 V range. These runs were performed according to the electrochemical procedure already described.

2.4.2. Transmission electron diffraction

The crystallographic structure of small Ag aggregates prepared by electrochemical methods was determined by TED. This technique was preferred to other X-ray diffraction techniques which are not suitable for determining crystal morphology and relative orientation on unusually small crystalline aggregates. In such a case, macroscopic specimens for X-ray diffraction (10–100 mg) are usually made up of an extremely large number (10^{13}–10^{15}) of individual particles, where all morphological and orientational features, as they appear in the diffraction patterns, are necessarily smeared and masked by the random nature of their mutual orientations. TED, however, is ideally suited for focusing on individual crystal aggregates ($\pm 10^{-16}$ g) of the sample, thus leading to the possibility of conducting unequivocal morphological studies.

The electron diffractograms were obtained with a Siemens Elmiskop 101 electron microscope furnished with a liquid N_2 anti-contamination device and a cooling stage at 100 kV acceleration potential. Double-condenser illumination conditions were applied, with the first condenser lens fully energized and a 20 μm aperture fitted to the second lens [23]. In this way the influence of spherical aberration in the second condenser was kept to a minimum, and the irradiated regions of the specimens were restricted to very small surface areas (± 1 μm^2). Calibration of the microscope column to establish the diffraction constant was accomplished by recording electron diffraction patterns of vacuum-deposited Au films. Specimen preparation was carried out by electrodepositing Ag dendrites on Pt at $\eta = -0.58$ V in solution I. Ag dendrites were rinsed with Milli-Q* water and deposited on Au films.

2.4.3. Scanning tunneling microscopy

STM images of columnar and dendritic Ag electrodeposits prepared as described in Section 2.1 were acquired using a McAllister scanning tunneling microscope operating in ambient conditions. Pt + Ir tips used for STM imaging were made by cutting Pt + Ir wires 0.11 mm in diameter. The images were obtained by applying a 0.06 V bias voltage with the tip positive at a constant current of 1–2 nA.

The STM calibration was performed through the HOPG surface lattice. At the highest resolution (4 nm × 4 nm) the typical hexagonal array of C atoms, where only three out of the six C atoms in the graphite lattice leading to nearest-neighbor distances of 0.24 ± 0.02 nm, was observed. In addition, the honeycomb structure with a C–C distance of 0.14 ± 0.02 nm was also resolved.

Data were acquired at a fully automated workstation and stored as digitized images with 200 × 200 or 400 × 400 pixels.

2.5. X-ray photoelectron spectroscopy

XPS analysis was carried out in an ultrahigh vacuum (UHV) chamber at a base pressure lower than 10^{-9} Torr using Vacuum Generator Scientific ESCA 3 Mark II equipment. XPS data were obtained with Mg Kα radiation (1253.6 eV) at an angle of 60° between the surface normal and the analyser lens in order to increase the surface sensitivity of the spectra. The collection time was between 20 s and 60 s. WE samples coated with columnar Ag were removed from the cell by holding the potential at different preset E_h values, rinsing with N_2-saturated Milli-Q* water and drying under N_2.

3. Results

3.1. Characterization of Ag working electrodes

3.1.1. Pb underpotential deposition

The Pb UPD–anodic stripping voltammograms recorded on columnar Ag electrodes (Fig. 1(a)) show a pair of small broad peaks covering the −0.24 V to −0.32 V range [17]. The Pb UPD–anodic stripping voltammograms of Ag dendritic electrodes (Fig. 1(b))

exhibit a large sharp pair of peaks located at −0.3 V with shoulders at −0.26 V. In addition, a small pair of peaks is also observed at −0.4 V, a potential which is close to the Pb/Pb^{2+} reversible electrode potential. The voltammograms depicted in Fig. 1(b) closely resemble those recorded at a stepped Ag(111) surface [24,25].

3.1.2. Transmission electron diffraction data

A typical TED pattern of Ag dendrites mounted onto fine-grained Au polycrystalline films (Fig. 2) shows continuous rings corresponding to the polycrystalline Au film, while the discrete spots correspond to the Ag dendrites. The following features can be distinguished from the TED patterns.

Only Ag(220) single-crystal reflections are observed. This means that Ag(220) and the corresponding Ag(110) planes are normal to the substrate surface, i.e. the [220] and [110] vectors are normal to the electron beam direction. No four-fold symmetry is observed, in agreement with the preceding conclusion.

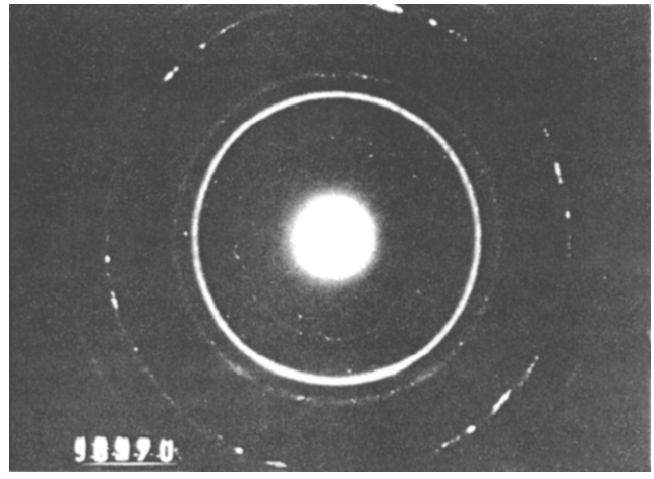

Fig. 2. Transmission electron diffractogram of a Ag dendritic deposit from solution I at $\eta_c = -0.58$ V and 25°C.

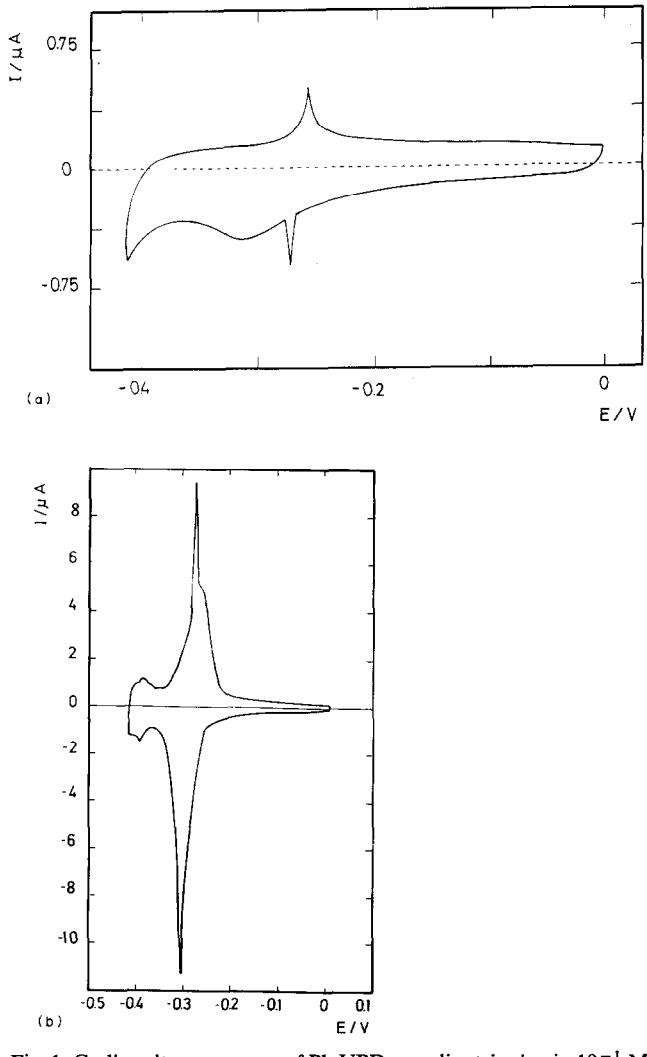

Fig. 1. Cyclic voltammograms of Pb UPD–anodic stripping in 10^{-1} M $NaClO_4 + 5\times10^{-3}$ M $HClO_4 + 10^{-2}$ M $Pb(ClO_4)_2$ at 0.01 V s^{-1} and 25°C: (a) columnar Ag WE; (b) dendritic Ag WE.

Other intense reflections of Ag(111), Ag(200) and Ag(311) are conspicuously absent from the diffraction patterns. This precludes an unequivocal definition of the orientation of crystallites, since with only two points available ((200) and (000)) it is not possible to define the position of the [220]-pole axis around which crystallites can adopt any orientation.

The main set of Ag(220) reflections are related to each other by a six-fold axis of symmetry. In addition, each major reflection shows a weaker satellite at about 10°, and even weaker streaks within this 10° range. The presence of hexagonal symmetry in the diffraction patterns immediately indicates the growth of ordered Ag aggregates, crystallographically related to each other by the six-fold axis, as no possible orientation of an individual cubic single crystal can give rise to a set of 60° reflections related to Ag(220). Furthermore, secondary nucleation may be responsible for the weaker satellite reflections shown up in such a regular fashion.

3.1.3. Scanning tunneling microscopy data

STM images of the Ag electrodeposits grown at $\eta_c = -0.06$ V (Fig. 3) show nanometer-size elements which correspond to the column tips forming the deposit structure [17]. The average size of these rounded elements is close to 20 nm. In contrast with other columnar structures, such as those resulting from vapor-deposited Au films [26], no preferred orientation of the small columns are observed in the STM images. The structure of the Ag electrodeposits grown at this potential closely resembles the columnar structure of

Au and Pt electrodeposits grown from the electroreduction of their respective hydrous oxides [27,28].

The surfaces of dendritic Ag electrodeposits grown at $\eta_c = -0.58$ V show large differences in height, making the STM imaging of these specimens difficult. Nevertheless, stable tunneling conditions can be obtained in small domains, typically of dimensions 40 nm $\times$ 40 nm. These images show terraces and multiple-height steps (Fig. 4(a)) intersecting at 30°, 60° and 120° (Fig. 4(b)). The surface topography of these domains appears to be consistent with a stepped Ag(111) surface.

3.2. *Voltammetric data related to Cd electrodeposition–anodic stripping*

Conventional Cd UPD voltammetry shows at least two sharp conjugated pairs of peaks and the contribution of an additional broad pair of peaks on both columnar (Fig. 5(a)) and dendritic (Fig. 9(a) below) Ag. It should be noted that the voltammetric features mentioned above are better defined for dendritic Ag electrodes. Generally, these results agree with those previously reported for Cd atom electrodeposition on both Ag polycrystalline surfaces and well-defined single crystal faces [9,10].

The charge resulting from the voltammograms exceeds the charge density of the Cd UPD ML. However, it is possible to evaluate that the charge density of the Cd UPD ML when E_{sc} is close to -0.585 V.

3.2.1. *Cd underpotential deposition–anodic stripping on columnar Ag electrodeposits*

The Cd UPD–anodic stripping CVs at compact columnar Ag electrodeposits run at 0.02 V s^{-1} from 0.150 V to -0.585 V (Fig. 5) in solution II show a continuous increase in the cathodic current with a small current inflection (not seen in the Fig. 5) near the lower switching potential E_{sc} and a trend to displaying a hump in the -0.165 V to -0.385 V range. Conversely, the reverse potential scan exhibits broad peaks Ia at -0.425 V and IIa at -0.2 V. The values of the area and of the roughness factor for the columnar Ag electrodeposit ($A = 0.074$ cm^2 and $R = 2.7$ respectively) have been calculated from the anodic and the cathodic voltammetric charges Q_a and Q_c, assuming $q_M = 0.42$ mC cm^{-2} for the Cd ML charge density, a figure which results from a process involving two electrons per site per adsorbate species on an ideal smooth surface.

Similar runs made at different E_{sc} show that both Q_a and Q_c decrease as E_{sc} is positively shifted, although $Q_a/Q_c \approx 1$ irrespective of E_{sc}. The effect of E_{sc} on Q_a and Q_c is accompanied by changes in the reversibility of the anodic and cathodic reactions, as can be seen, for instance, by plotting both θ_a and θ_c vs. E_{sc} (Fig. 6), where θ_a and θ_c are the degrees of Ag

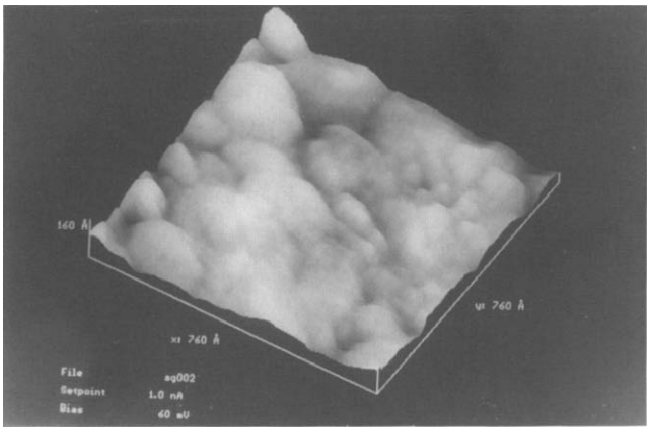

Fig. 3. Three-dimensional STM image (76 nm $\times$ 76 nm) of a columnar Ag electrodeposit from solution I at $\eta_c = -0.06$ V.

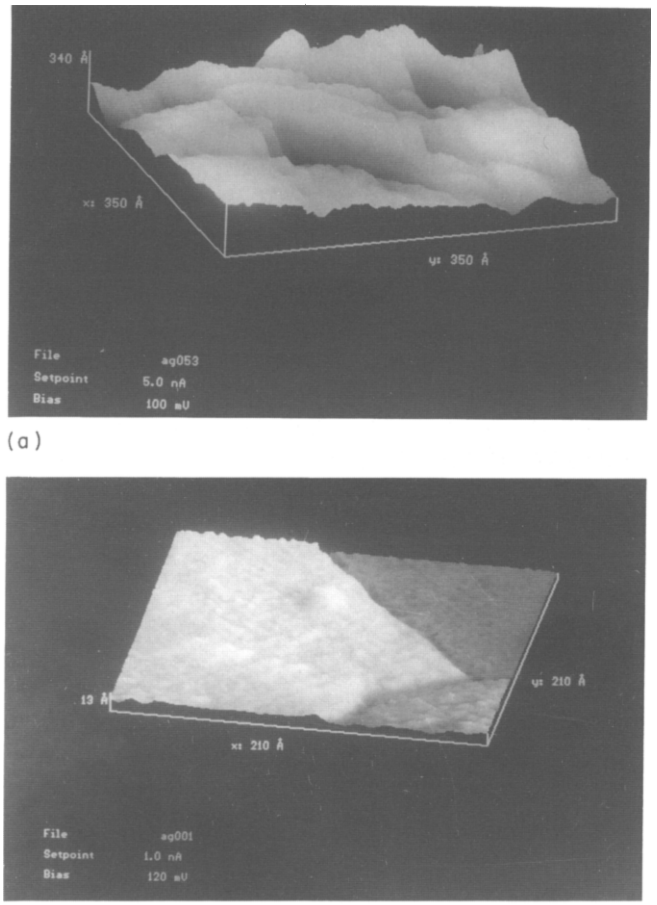

Fig. 4. STM images of dendritic Ag electrodeposits from solution I at $\eta_c = -0.58$ V: (a) three-dimensional image (35 nm $\times$ 35 nm); (b) top view image (21 nm $\times$ 21 nm).

surface coverage assigned to Cd atoms at the anodic and cathodic reaction respectively. These values of θ are referred to $q_{ML} = 0.42$ mC cm^{-2}. Within the same range of θ, the θ_c vs. E_{sc} plot shows a continuous decrease from unity to zero, whereas the θ_a vs. E_{sc} plot presents a sigmoid shape. This difference suggests that processes involved in each Cd UPD–anodic stripping cycle are not strictly complementary. The reason for this has to be considered in terms of a rather complex reaction, which is anodic or cathodic or both.

3.2.1.1. The influence of E_h on Cd anodic stripping voltammograms. The Cd anodic stripping voltammograms are sensitive to E_h and t_h. Let us consider the influence of t_h on the voltammograms at different E_h. Thus, when $E_h = -0.39$ V, i.e. for $\theta_c = 0.4$ (Fig. 7), from the comparison between the voltammograms run

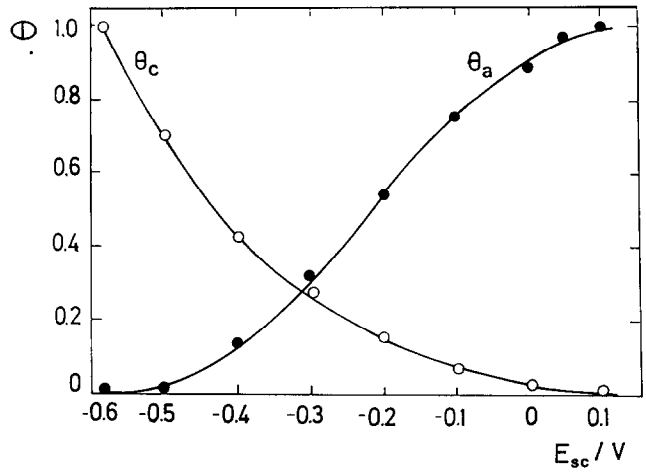

Fig. 6. Plots of θ_a vs. E_{sc} and θ_c vs. E_{sc} for Cd UPD–anodic stripping in solution II at 0.02 V s^{-1} and 25°C for columnar Ag WE.

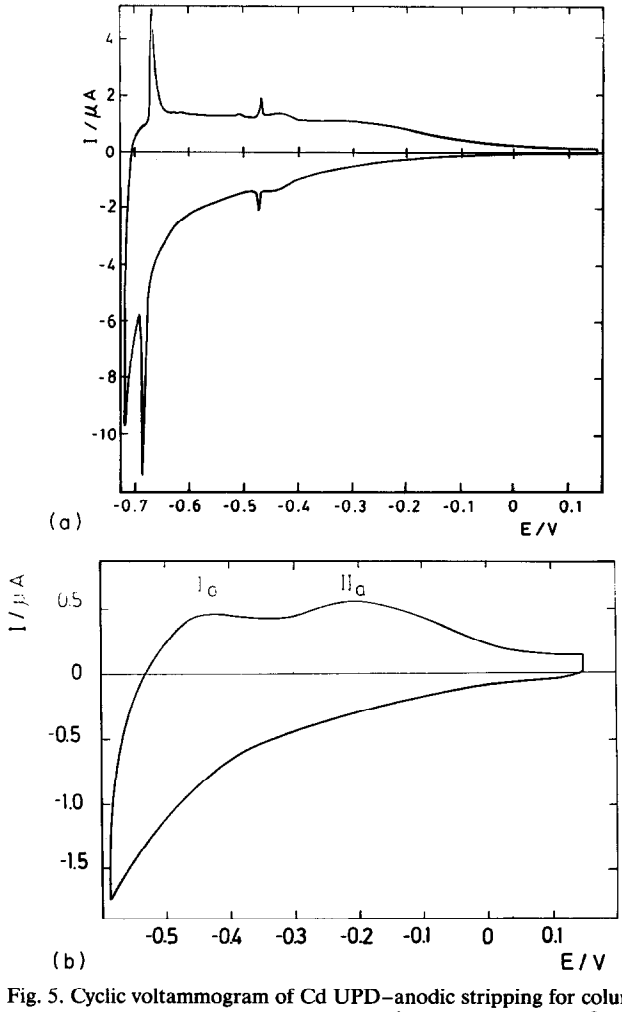

Fig. 5. Cyclic voltammogram of Cd UPD–anodic stripping for columnar Ag WE in solution II at 0.02 V s^{-1}, $q_{Ag} = 50$ mC cm^{-2} and 25°C: (a) $E_{sc} = -0.705$ V; (b) $E_{sc} = -0.585$ V.

after holding the potential at E_h for t_h and CV 1 without holding the potential at E_h (Fig. 5(b)), the following features can be observed. For 5 min $< t_h <$ 60 min, the decrease in the height of peak Ia is comparable to the increase in the height of peak IIa (Fig. 7(a)). Otherwise, for $t_h > 1$ h peak IIIa at ca. 0.1 V develops and its height increases with t_h (Fig. 7(b)). Finally, for $t_h > 4$ h, peaks IIa and IIIa tend to overlap and a stationary CV is approached (Figs. 7(c) and 7(d)). Then the voltammetric charge distribution results in 0.2 ML for peak Ia (weakly bound adsorbate) and 0.8 ML for other contributions (strongly bound adsorbate), leading to $\theta_a \approx 1$ ML. This behavior is opposite to that found for conventional Cd UPD–anodic stripping CVs, as in this case about 80% of Cd UPD appears as a strongly bound adsorbate.

Similar runs were made by setting $E_h = -0.575$ V, i.e. $\theta_c = 0.96$ (Fig. 8), where it was found that, for 1 min $< t_h <$ 10 min, the increase in the height of peaks Ia and IIa are about the same, nearly irrespective of t_h (Fig. 8(a)). However, for $t_h > 10$ min (Fig. 8(b)), peak Ia turns into the sharp peak I$'_a$ at -0.365 V. These changes become more noticeable for $t_h \approx 4$ h (Fig. 8(c)) where the height of peak I$'_a$ increases and its potential shifts positively as t_h is increased. Furthermore, peak IIIa at 0.05 V and complex peak Ic' at ca. -0.4 V can also be observed. The value of Q_a becomes equivalent to 1.9 ML, and CV features obtained for $t_h \geq 4$ h substantially differ from those found for $t_h = 0$. For $t_h \approx 14$ h (Fig. 8(d)), CV 1 shows a well-defined peak I$'_a$, and after ca. five CVs the features closely resembles those obtained in the Cd UPD–anodic stripping voltammogram run on a dendritic Ag electrode under comparable conditions, as described below.

3.2.2. Cd underpotential deposition–anodic stripping on dendritic Ag electrodeposits

The Cd UPD–anodic stripping CVs resulting from dendritic Ag electrodeposits at 0.02 V s^{-1} in the 0.15 V to −0.58 V range (Fig. 9(a)) show symmetric conjugated pairs of peaks in the −0.425 V to −0.6 V range. The conjugated pair of peaks at −0.46 V is very sharp, and the corresponding θ_a and θ_c vs. E_{sc} plots (Fig. 9(b)) are much more symmetrical than those resulting from compact columnar-structured Ag electrodeposits (Fig. 6). From these results it can be concluded that the Cd UPd–anodic stripping processes on dendritic Ag WEs behave as reversible surface electrochemical reactions.

From the values of Q_a and Q_c, and assuming q_M = 0.42 mC cm^{-2} for the Cd monolayer charge density, the area and the roughness factor of the dendritic Ag electrodeposit are obtained as $A = 0.15$ cm^2 and R = 5.5. These figures are twice the values of those found for columnar Ag electrodeposits.

3.2.2.1. The influence of E_h on Cd anodic stripping voltammograms. Runs including a potential holding at $E_h = -0.40$ V, i.e. $\theta_c \approx 0.27$, show that the first CV after holding the potential at E_h remains almost unchanged for $t_h < 1$ h (Fig. 10(a)), whereas for $t_h > 1$ h it exhibits a decrease in both height and sharpness of all peaks compared with the first CV obtained without holding the potential at E_h. Simultaneously, the broad peak IIIa at 0.025 V starts to grow (Fig. 10(b)) and its charge increases with t_h, in contrast with the charge involved in the −0.425 V to −0.6 V range. However, for $t_h > 10$ h a steady CV with $\theta_a \approx 1$ ML is attained. This surface coverage is distributed as θ_{Cd} (peak IIIa) ≈ 0.27 ML and θ_{Cd} (other contributions) ≈ 0.73 ML. Hence the relative contribution of weakly bound Cd species to dendritic Ag WEs has been considerably increased compared with compact columnar Ag WE (see Section 3.2.1.1).

Similar runs were performed by setting E_h = −0.47 V, i.e. $\theta_c \approx 0.6$ (Fig. 11). For $0 < t_h < 30$ min, peak I'_a at −0.365 V can be observed (Fig. 8(c)) (see Section 3.2.1.1), and for $t_h > 1$ h it develops a small shoulder at ca. −0.275 V and peak IIIa starts to grow at 0.025 V. Finally, for $t_h > 14$ h peaks Ia′, IIa′ and IIIa are seen (Fig. 11), and after a very prolonged cyclic voltammetric treatment, the entire CV approaches that shown in Fig. 9(a). Throughout these experiments, the value of θ_a continuously increases from 1 ML to 2 ML as $t_h \to \infty$. Results from these runs are assembled in Table 1 including the value of Q_a for peak Ia and the

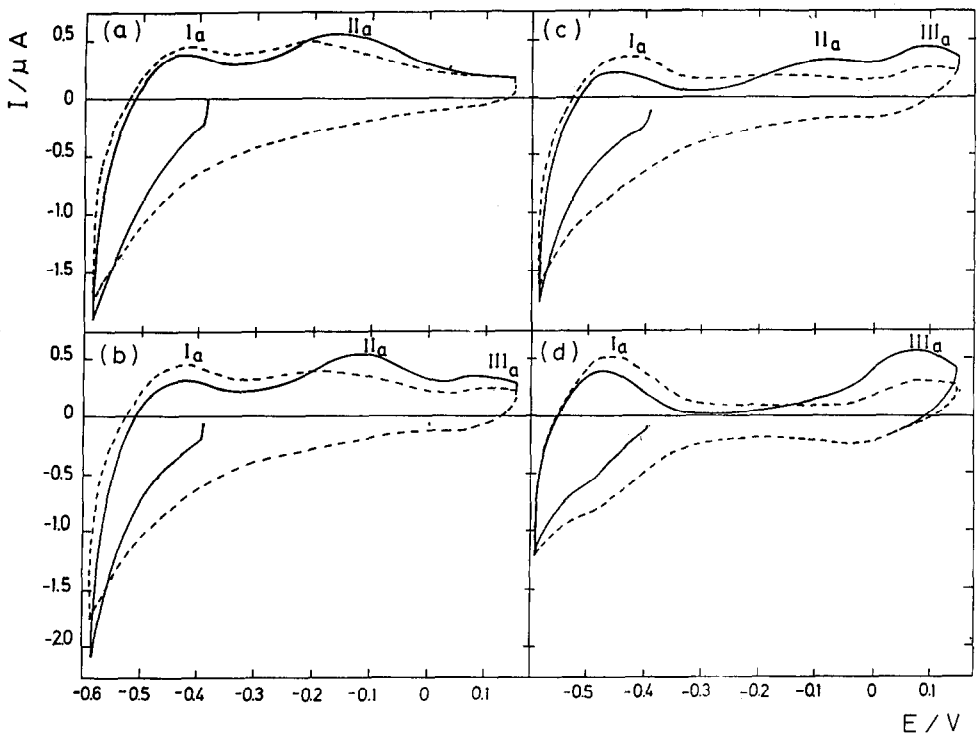

Fig. 7. Cyclic voltammograms of Cd UPD–anodic stripping for columnar Ag WEs, at 0.02 V s^{-1} including a potential holding at $E_h = -0.39$ V applied in the negative-going potential scan during different times t_h at 25°C (——— CV 1; — — — CV 2): (a) t_h = 16 min; (b) t_h = 2 h; (c) t_h = 4 h; (d) t_h = 14 h.

$Q_t^{upd}/Q_{t=0}^{upd}$ ratio, where Q_t^{upd} and $Q_{t=0}^{upd}$ stand for the residual and the initial UPD Cd charges respectively.

Voltammograms resulting from $E_h = -0.575$ V, i.e. $\theta_c \approx 1$, largely resemble those obtained on compact columnar Ag WE at the same E_h, although the voltammetric features of the dendritic Ag WE depend on whether t_h is smaller or larger than a critical time t_c ($t_c \approx 10$ min) (Fig. 12). For $t_h < t_c$ (Fig. 12(a)) the Cd anodic stripping charge resulting from CV 1 exceeds that derived from the CV without holding the potential at E_h, although the shape and distribution of peaks, including peak I'_a at -0.365 V, remain almost the same. Otherwise, for $t_h > t_c$ (Fig. 12(b)) the height of peak Ia′ increases, but a poorer definition of Cd UPD peaks compared with those shown in Fig. 12(a) can be seen. For $t_h > 1$ h peak I'_a is defined, including its splitting into two peaks centered at -0.355 V and at -0.375 V (Fig. 12(c)). These CV features are also very sensitive to E_h. Finally, a stationary Cd anodic stripping voltammogram is attained for $t_h \to 12$ h, and in this case $\theta_{Cd} \to 2$ ML. It should be noted that the conjugated pair of peaks IIIa/IIIc at ca. 0.025 V and θ_{Cd} values slightly greater than 2 ML can be obtained for $t_h > 10$ h. Data derived from these runs are summarized in Table 2.

For both columnar and rough Ag WEs, neither shape nor voltammetric charge changes have been observed after 24 h potential cycling at 0.02 V s^{-1} between 0.15 V and -0.585 V, i.e. in the Cd UPD–anodic stripping potential range. These results suggest that both the area and the structure of the Ag surface remain stable during long-term potential cycling. Presumably, the Ag surface atom mobility becomes sufficiently fast to expect any long-time-range surface roughness decay. Conversely, the CV changes produced by short-time potential cycling indicate possible electrode surface changes mainly caused by potential holding at E_h during t_h. These changes may reflect

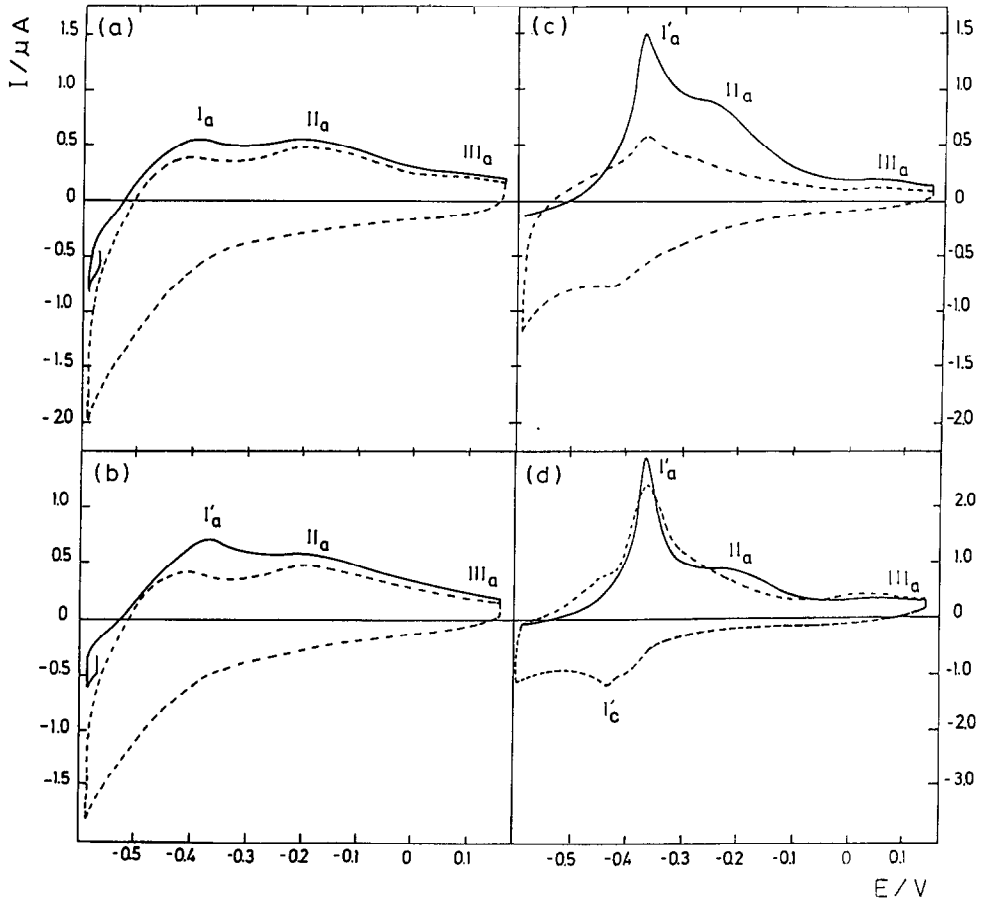

Fig. 8. Cyclic voltammograms of Cd UPD–anodic stripping for columnar Ag WEs at 0.02 V s^{-1} including a potential holding at $E_h = -0.575$ V applied in the negative-going potential scan during different times t_h at 25°C (——— CV 1; — — — CV 2): (a) $t_h = 1$ min; (b) $t_h = 10$ min; (c) $t_h = 4$ h; (d) $t_h = 14$ h.

different types of interactions between surface Ag and Cd atoms. The surface roughness relaxation probably occurs at a rate close to the Ag electrodeposition rate.

3.2.2.2. The influence of E_h on the Cd underpotential deposition–anodic stripping voltammetric charge. Charge evaluation from voltammograms (Figs. 13 and 14) was attempted for dendritic Ag WEs ($q_{Ag} = 50$ mC cm^{-2}) for $t_h = 15$ min (Figs. 13(a) and 14(a)) and $t_h = 30$ min (Figs. 13(b) and 14(b)) covering the -0.35 V $< E_h < -0.588$ V range by setting all variables except E_h. From these Cd anodic stripping voltammograms (Fig. 13), a decrease in charge Q_- at the negative potential side of peak Ia, which corresponds to a decrease in the amount of weakly bound Cd, and an increase in charge Q_+ at the positive potential side of peak Ia, which represents an increase in the amount of strongly bound Cd, are observed. Evaluation of these charges was attempted by means of the scheme illustrated in the inset to Fig. 14(a). In this case, the Q_- vs. E_h (Figs. 14(a) and 14(b), open circles) and Q_+ vs. E_h (Figs. 14(a) and 14(b), solid circles) plots show two interesting features irrespective of t_h, namely an increase in Q_+ when $E_h > E_t$, where $E_t \approx -0.4$ V is a threshold potential value, and a change in Q_- over a rather small E_h range, which goes through a maximum value at $E_h \approx -0.5$ V. Thus Q_+ and Q_- increase with a common slope from E_t up to $E_h \approx -0.5$ V, indicating that the decrease in the weakly bound Cd UPD atoms is accompanied by an increase in the strongly bound Cd UPD atoms. However, the Q_+ increase from E_h to E_r is due not only to the increase in peak Ia but also to the increase in peak I'$_a$, whose contribution arises from the removal of Cd atoms from the Cd + Ag surface.

3.3. Cd underpotential deposition–anodic stripping on Cd + Ag alloy

Voltammograms of a Cd + Ag alloy (α phase) WE in solution II run at $v = 0.02$ V s^{-1} covering different E_{sc} and E_{sa} values (Fig. 15) show a first region extending from -0.325 V to -0.6 V, which is the main Cd

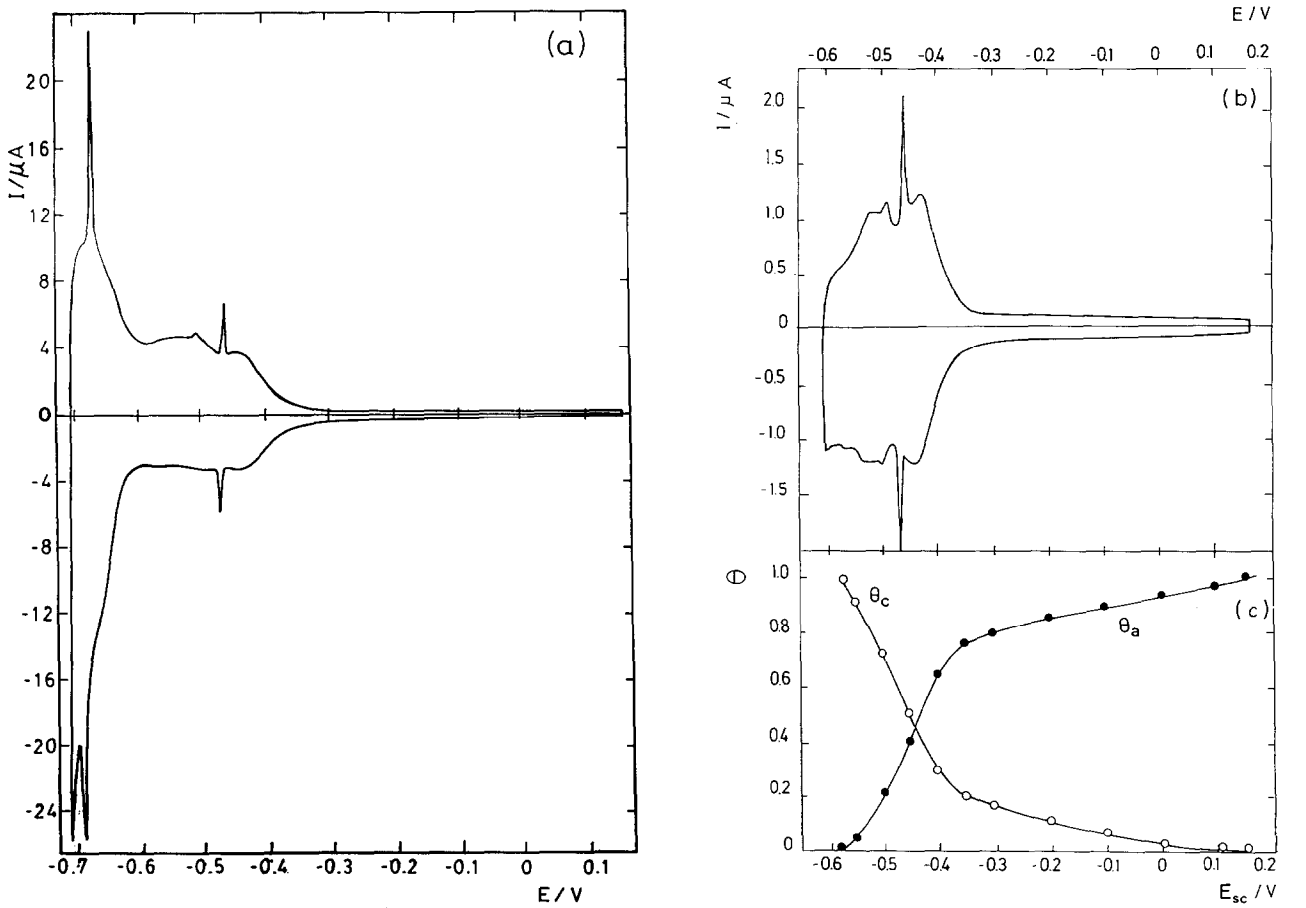

Fig. 9. Cyclic voltammograms of Cd UPD–anodic stripping for dendritic Ag WEs in solution II at 0.02 V s^{-1}: (a) $E_{sc} = -0.705$ V; (b) $E_{sc} = -0.585$ V. (c) θ_a vs. E_{sc} and θ_c vs. E_{sc} plots related to (b). Temperature, 25°C.

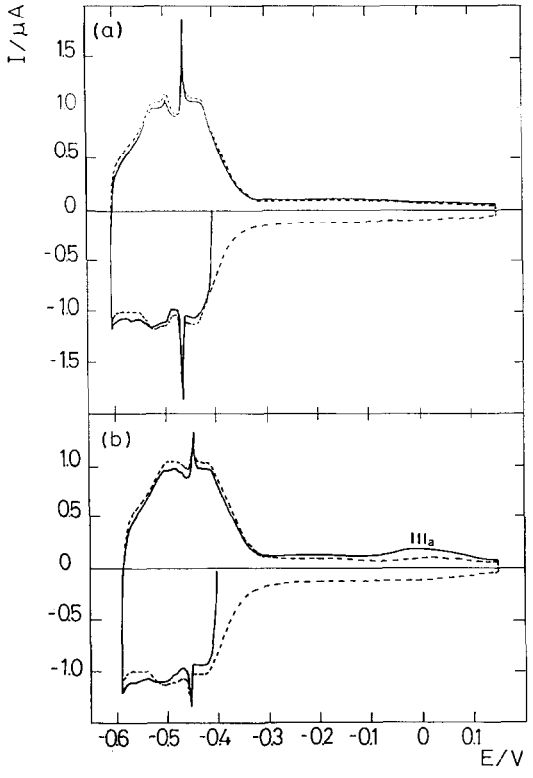

Fig. 10. Cyclic voltammograms of Cd UPD–anodic stripping for dendritic Ag WEs at 0.02 V s^{-1} including a potential holding at $E_h = -0.40$ V applied in the negative-going potential scan during different times t_h (——— CV 1; — — — CV 2): (a) $t_h = 30$ min; (b) $t_h = 3$ h. Temperature, 25°C.

UPD–anodic stripping potential range on Ag, and a second region from −0.1 V to 0.2 V, where three broad symmetric peaks related to the anodic stripping

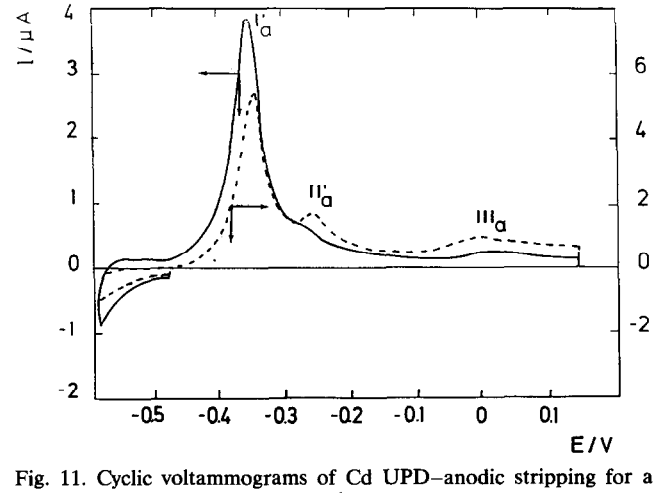

Fig. 11. Cyclic voltammograms of Cd UPD–anodic stripping for a dendritic Ag WEs at 0.02 V s^{-1} including potential holding at $E_h = -0.47$ V applied in the negative-going potential scan for different times t_h at 25°C: (———) $t_h = 3$ h; (— — —) $t_h = 15$ h.

TABLE 1. Voltammetric data obtained with dendritic Ag WEs which were held at $E_h = -0.47$ V for different times t

t/s	Q_t/ML	Q'_{Ia}/ML	$Q_t^{upd}/Q_{t=0}^{upd}$
0	1	0	1
300	1.04	0.02	1
600	1.07	0.10	0.968
900	1.07	0.15	0.915
1800	1.12	0.30	0.820
3600	1.24	0.64	0.592
7200	1.78	1.29	0.485
10920	1.58	1.21	0.367
53985	2.04	2.02	0.020

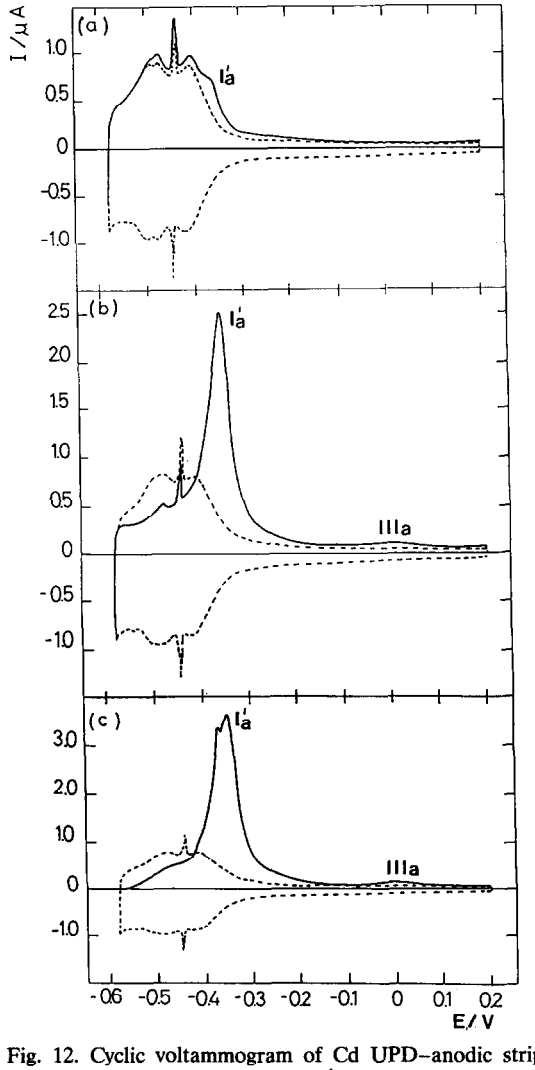

Fig. 12. Cyclic voltammogram of Cd UPD–anodic stripping for a dendritic Ag WEs at 0.02 V s^{-1} including potential holding at $E_h = -0.575$ V applied in the negative-going potential scan for different times t_h at 25°C (——— CV 1; — — — CV 2): (a) $t_h = 5$ min; (b) $t_h = 30$ min; (c) $t_h = 76$ min.

TABLE 2. Voltammetric data obtained with dendritic Ag WEs which were held at $E_h = -0.575$ V for different times t

t/s	Q_t/ML	Q'_{Ia}/ML	$Q_t^{upd}/Q_{t=0}^{upd}$
0	1	0	1
60	1.07	0	1
180	1.11	0.12	0.997
300	1.15	0.17	0.983
600	1.16	0.26	0.901
900	1.29	0.42	0.874
1800	1.50	0.85	0.684
3720	1.48	0.93	0.549
5400	1.81	1.32	0.488
9000	2.0	1.67	0.333
14400	2.18	1.88	0.297
46200	2.55	2.38	0.157

of Cd atoms from the Cd + Ag bulk alloy are found. Those peaks assigned to electrochemical reactions at Cd + Ag bulk alloy are definitely absent at all types of Ag WE, even when E_{sc} is set in the Cd overpotential electrodeposition range (Fig. 16).

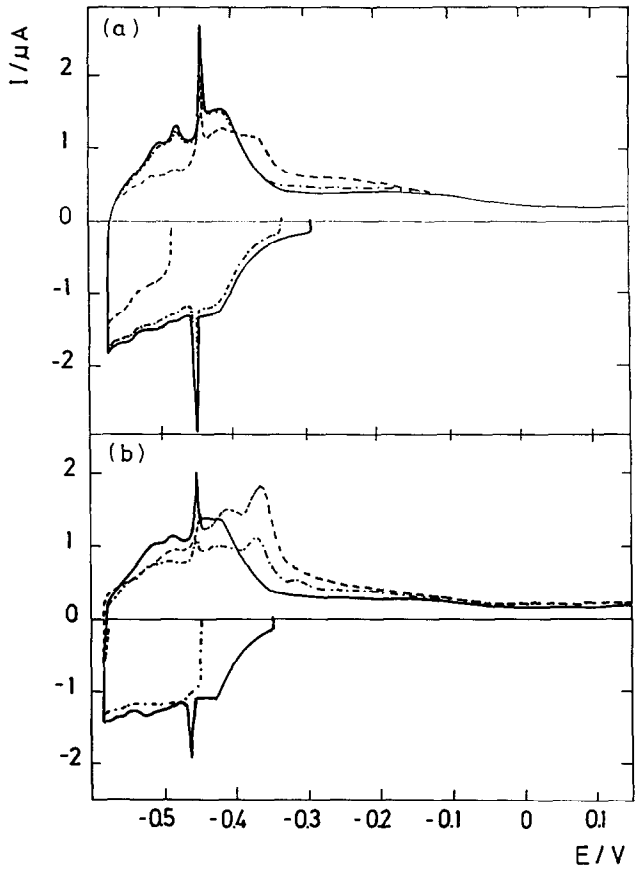

Fig. 13. Cyclic voltammograms of Cd UPD–anodic stripping for dendritic Ag WEs at 0.02 V s^{-1}: (a) $E_h = -0.30$ V (———), $E_h = -0.34$ V (·–·–·) and $E_h = -0.49$ V (– – –) at $t_h = 15$ min; (b) $E_h = -0.35$ V (———), $E_h = -0.45$ V (·–·–·) and $E_h = -0.59$ V (– – –) at $t_h = 30$ min. Temperature, 25°C.

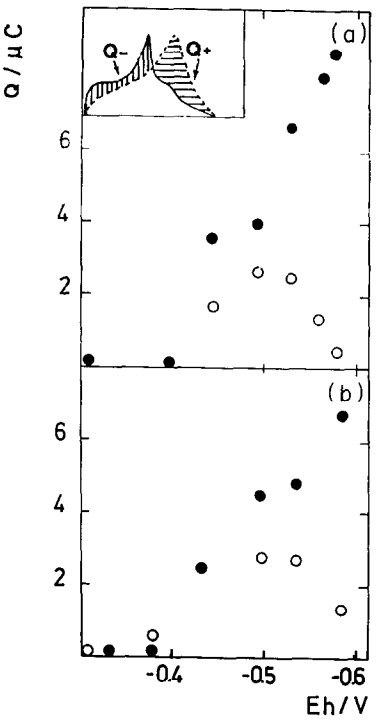

Fig. 14. Charge decrease Q_- (○) and charge increase Q_+ (●) vs. holding potential E_h for (a) $t_h = 15$ min and (b) $t_h = 30$ min. Data correspond to the cyclic voltammograms shown in Fig. 13. A scheme for the calculation of Q_- and Q_+ is shown in the inset. Apparent electrode area, 0.04 cm^2; temperature, 25°C.

3.4. X-ray photoelectron spectra

X-ray photoelectron spectra of columnar-Ag-coated WEs, which were held at $E_h = -0.57$ V for $t_h = 10$ h in solution I, show the 367.9 eV signal which corresponds to Ag and the 404.8 eV signal of Cd which emerges as a weak signal from the background [29]. According to X-ray photoelectron spectra, the amount of Cd on this type of Ag substrate can be estimated as that expected from $\theta_{Cd} \approx 1$ ML although it lies in the detection limit of the technique. Similar results were

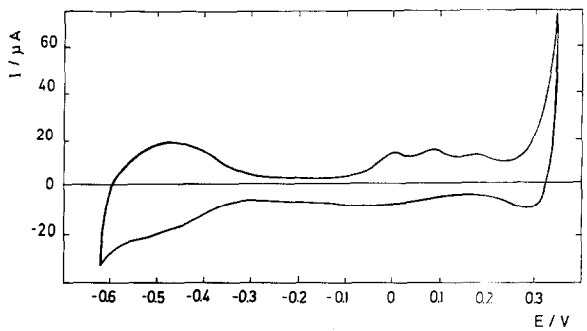

Fig. 15. Cyclic voltammograms of Cd UPD–anodic stripping on a Cd+Ag alloy WE in solution II at 0.02 V s^{-1}: apparent electrode area, 1 cm^2; temperature, 25°C.

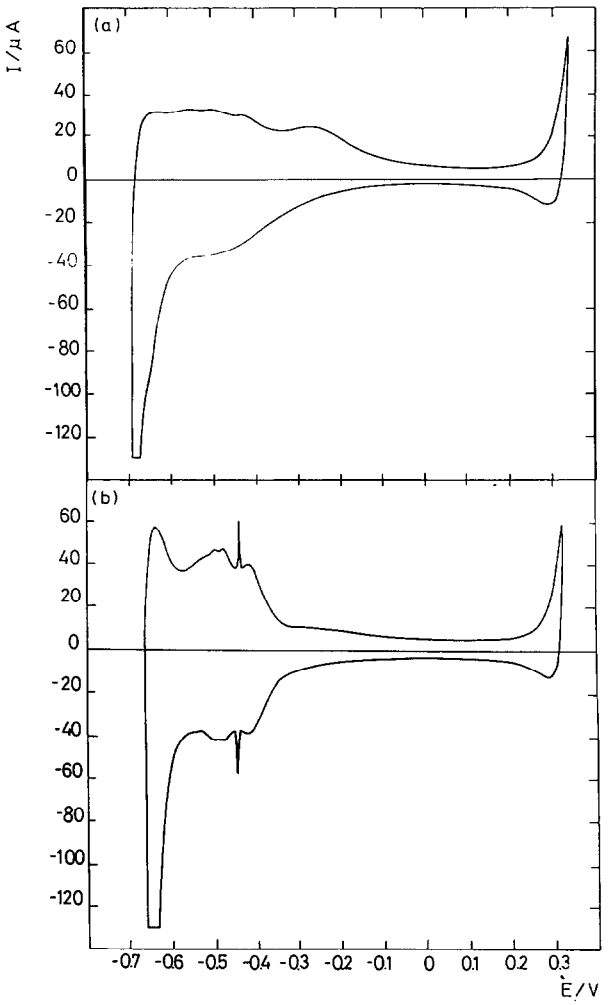

Fig. 16. Cyclic voltammograms of Cd UPD–anodic stripping from $E_{sc} = -0.65$ V to $E_{sa} = 0.31$ V in solution II at 0.02 V s^{-1}: (a) Columnar Ag WE (apparent electrode area 0.89 cm^2); (b) dendritic Ag WE (apparent electrode area 1.15 cm^2). Temperature, 25°C.

obtained after holding the potential at E_h for $t_h = 24$ h. After Ar ion bombardment, the Cd signal completely disappears at ca. 0.5 nm. This result indicates that Cd penetration depth into the substrate is no greater than 2 ML.

4. Discussion

4.1. The probable structures of Ag electrodeposits

The structure of columnar metal electrodeposits has been thoroughly discussed in recent papers [17,19]. It consists of a collection of nanometer-size columns with smooth tips. The fluctuations in the height of columns lead to a self-affine fractal surface for lengths larger than the average columnar size [19]. However, in this case, as the Cd and Pb atom sizes are smaller than the average columnar size, the fractal character of these surfaces is not observed for the electrodeposition of those metal atoms and the Ag substrate behaves as a Euclidean polycrystalline surface.

Furthermore, the structure of dendritic Ag electrodeposits can be described in terms of self-similar fractals for lengths larger than the size of the smaller branch, which is in the micrometer range [18]. In addition, the individual branches are stepped single crystals with (111) faces as revealed by TED and STM measurements respectively. Thus Cd and Pb atom electrodeposition occurs on crystalline surfaces formed by Ag(111) terraces and steps.

4.2. The multiplicity of Cd underpotential deposition peaks for $\theta_c \leq 1$ and possible surface structures

The structure of Ag electrodeposits at the nanometer level explains the voltammetric characteristics of Cd and Pb electrodeposition–anodic stripping peaks. From the electrochemical standpoint, the main difference between columnar and dendritic Ag electrodeposits lies in the definition and the reversibility of Cd UPD–anodic stripping peaks appearing in the −0.59 V to 0.15 V range. For both Ag substrates the voltammograms show a low Cd UPD range from −0.59 V to ca. −0.4 V where complementary voltammetric peaks are observed, and a high Cd UPD range from −0.4 V to 0.15 V where the voltammetric peaks are due to alloyed Cd, as confirmed by CV data on Cd + Ag alloys (Fig. 15). For columnar Ag electrodeposits the broad current peaks recorded for Cd and Pb UPD–anodic stripping voltammograms are consistent with a disordered polycrystalline surface. Conversely, voltammograms corresponding to dendritic Ag electrodeposits exhibit sharp and reversible current peaks which closely resemble those obtained on stepped Ag(111) single crystals [10,24,25], in agreement with STM and TED data.

A model for the exchange between Cd atoms at the surface and Ag atoms at the first Ag layer is shown schematically in Fig. 17 (schemes A and B). In this model 1 ML of Cd can produce two layers of a 1:1 Cd + Ag alloy. Furthermore, a new UPD Cd ML can be formed on top of the first Cd + Ag layer (schemes C and D). Accordingly, the anodic stripping of Cd species from the alloy surface should differ from the anodic stripping of a Cd UPD on Ag, as the Cd atoms are in contact with Ag and Cd atoms rather than exclusively with Ag atoms of the substrate. Consequently, a different anodic stripping voltammogram should be observed. The strong distortion of the anodic stripping voltammogram produced by cathodizing supports this assumption. Thus, as the potential is positively shifted from E_r to 0.15 V, the Cd UPD monolayer stripping from Cd + Ag alloy should occur first, followed by

removal of Cd atoms from the Ag + Cd surface. This process is related to peak I'_a, which is located slightly positive with respect to the anodic stripping peak of the strongly bound Cd UPD atoms on Ag. Finally, the Cd atoms lying in the second Cd + Ag layer (schemes C and D) are removed at more positive potentials; this process is assigned to peak III'_a. This model admits that the overall Cd stripping charge is equivalent to 2 ML.

4.3. Kinetics of dermalloy formation

Let us consider the potentiostatic formation of the Cd + Ag dermalloy for $0.6 < \theta_{Cd} < 1$. From experimental results it was concluded that a progressive decrease in the amount of weakly bound Cd UPD atoms is observed irrespective of the Ag electrode type. This decrease corresponds to increase in alloyed Cd which is stripped off at potentials even more positive than the anodic stripping of the strongly bound UPD Cd. The rate of penetration of Cd atoms at the dermalloy level can be obtained by assuming that the process implies Cd atom "diffusion" through the first Ag atom layer of a grain-boundary-free surface layer. For such an "unidirectional diffusion" $n(t)$, the number of Cd atoms on the Ag surface at time t is related to the number $n(t=0)$ of Cd atoms present on the Ag surface at $t=0$ by [30]

$$n(t) = n(t=0)\ \mathrm{erf}\left[(a/4Dt)^{1/2}\right] \qquad (1)$$

where D is the diffusion coefficient of the slowest moving reacting entity and a is the diffusion layer thickness. By expressing $n(t)$ in terms of the corresponding voltammetric charge, the following equation is obtained:

$$Q_c/Q_{c,0} = \mathrm{erf}\left[(a/4Dt)^{1/2}\right] \qquad (2)$$

where Q_c and $Q_{c,0}$ are the Cd UPD charges at $t=t$ and $t=0$ respectively. This equation is plotted as $Q_c/Q_{c,0}$ vs. t (Fig. 18) using experimental data obtained at $E_h = -0.47$ V and $E_h = -0.575$ V for a dendritic Ag WE. Experimental plots are compared with those resulting from eqn. (2) using $a = 0.29$ nm, $D = 5.0 \times 10^{-12}$ cm^2 s^{-1} for $E_h = -0.47$ V and $D = 7.7 \times 10^{-12}$ cm^2 s^{-1} for $E_h = -0.575$ V. In principle, the agreement between all the experimental data and the curve obtained using eqn. (2) with the parameters given above is reasonably good. The value $a = 0.29$ nm used in the calculation is equal to the lattice constant d_{Cd} of Cd, and it can be justified because in this case the diffusion of Cd atoms is limited to the first Ag atom layer, as has been proved by both electrochemical and XPS results. Otherwise, the value of D is in the order of magnitude of those reported for Cd atom diffusion on a Cd + Ag polycrystalline surface [9], but it is about 10^3 times larger than that reported for Cd + Ag alloying on single-crystal surfaces [10].

To understand the processes involved in the Cd + Ag dermalloy formation, values of the surface diffusion coefficients D_{sAg} and D_{sCd} of Ag and Cd respectively, found in the literature, can be discussed. D_{sAg} values between 10^{-12} and 10^{-9} cm^2 s^{-1} have been obtained by different experimental methods [31–33]. For D_{sAg} the smallest value is in accordance with the value resulting from eqn. (2); however, to the best of our knowledge, there are no available data for D_{sCd} in the literature to be compared with that found from eqn.

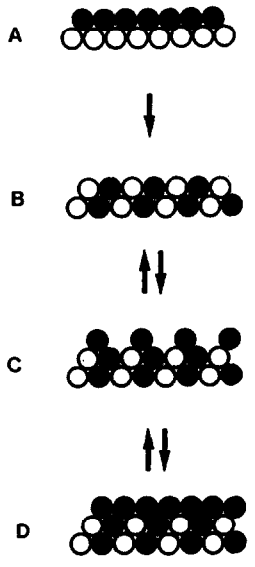

Fig. 17. Simplified scheme of possible Cd, Cd + Ag and Ag overlayer structures on Ag substrates and possible interconversion reactions: ● Cd atoms; ○ Ag atoms.

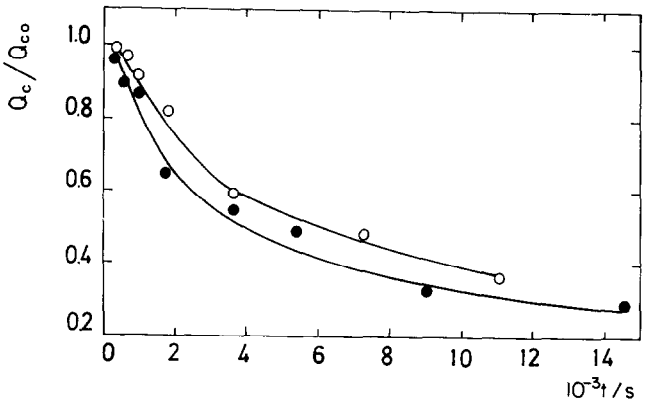

Fig. 18. $Q_c/Q_{c,0}$ vs. t plots: ○ $E_h = -0.47$ V; ● $E_h = -0.575$ V. Full curves correspond to data calculated using eqn. (2) as described in the text.

(2). Values of D_{sAg} and D_{sCd} can be estimated independently using the equation [34,35]

$$D_{sM} = 7.4 \times 10^2 \exp(-15T_m/T) + 1.4 \times 10^{-2} \exp(-6.5T_m/T) \quad (3)$$

where D_{sM} cm^2 s^{-1} is the surface diffusion coefficient of the metal M, T_m/K is the melting temperature of M and T/K is the working temperature. The validity of eqn. (3) has been proved through the evaluation of D_{sAu} for Au in electrolyte solutions using different experimental methods [36–38]. For $T = 298$ K, eqn. (3) gives $D_{sAg} = 2.13 \times 10^{-14}$ cm^2 s^{-1} and $D_{sCd} = 2.9 \times 10^{-8}$ cm^2 s^{-1}. The value of D_{sAg} resulting from eqn. (3) approaches the smallest D_{sAg} value determined in this work, i.e. $D_{sCd} \gg D_{sAg}$. Therefore the formation of the Cd + Ag surface alloy can be explained by an atom exchange mechanism and step growth [39,40] controlled by the surface mobility of Ag atoms at the surface Ag + Cd layer. Hence the kinetics of Cd + Ag dermalloy formation, particularly for $\theta_{Cd} \to 0$, would be determined by the Ag surface atom diffusion as the rate-controlling step. However, for $\theta_{Cd} > 0.6$, step motion at the substrate may contribute substantially to dermalloy formation as the Ag(111) dendritic surface provides a large number of steps. This explanation, which has been proposed for Pb + Ag alloying [12–14], is consistent with $\theta_{Cd} \approx 2$ ML.

Cd UPD at potentials close to E_r might also involve both two-dimensional (2D) and three-dimensional (3D) island formation, as the 2D ↔ 3D Cd adatom equilibrium at the monolayer level which has been found for different systems [41–43] probably occurs for Cd on Ag. For Pb UPD on Ag at potentials close to E_r the 2D → 3D surface atom rearrangement can be caused by strains generated by the different adsorbate and substrate atomic sizes [44–46]. In principle, this situation can be applied to the Cd + Ag system because of the different size of atoms, i.e. $d_{Cd} = 0.299$ nm and $d_{Ag} = 0.289$ nm. This type of process leading to uncovered Ag domains could favour dermalloy formation through a place-exchange mechanism with the predominant participation of weakly bound Cd and substrate atoms.

4.4 Possible bulk alloy formation

Under the experimental conditions of this work the contribution of Cd + Ag bulk alloying becomes negligible. However, as observed for $\theta_c > 1$, bulk Cd + Ag alloying would imply the penetration of Cd atoms into bulk Ag, a process which may either follow or accompany Cd + Ag dermalloy formation. Usually, bulk alloying occurs much more slowly than dermalloying. Bulk alloying kinetics can frequently be described through the formation of vacancies followed by atomic vacancy interdiffusion [47], as has recently been discussed for the penetration of Ag into bulk Pt [16]. Previously reported data about Cd + Ag alloy formation at different Ag single-crystal surfaces, as well as polycrystalline Ag [9,10] mostly based on the condition that $\theta > 1$, involved a penetration of Cd into bulk Ag which was equivalent to a Cd layer of thickness about 10 ML. Provided that grain-boundary-free Ag substrates were employed, these results are likely to be related to Cd + Ag bulk formation following a type of complex kinetics similar to that described previously.

Acknowledgments

Authors thank the Consejo Nacional de Investigaciones Científicas y Técnicas (CONICET, Argentina) for financial support of this work. AHC thanks CONICET, Argentina, and Universidad de La Laguna, Spain, for travelling grants to participate in this research work.

References

1 J. Bénard, Adsorption on Metal Surfaces. Studies in Surface Science and Catalysis, Vol. 13, Elsevier, Amsterdam, 1983.
2 E.B. Budevski in B.E. Conway, J.O'M. Bockris, E. Yeager, S.U.M. Khan and R.E. White (Eds.), Comprehensive Treatise of Electrochemistry, Vol. 7, Plenum, New York, 1983.
3 D.M. Kolb in H. Gerischer and C. Tobias (Eds.), Advances in Electrochemistry and Electrochemical Engineering, Vol. 11, Wiley, New York, 1978.
4 R. Adzic in H. Gerischer and C. Tobias (Eds.), Advances in Electrochemistry and Electrochemical Engineering, Vol. 13, Wiley, New York, 1984.
5 S. Szabó, Int. Rev. Phys. Chem., 10 (1991) 207.
6 R.C. Salvarezza and A.J. Arvia, Electrochim. Acta, 33 (1988) 1031.
7 R.C. Salvarezza, D.V. Vásquez Moll, M.C. Giordano and A.J. Arvia, J. Electroanal. Chem., 213 (1986) 301.
8 D.C. Alonzo and B.R. Scharifker, J. Electroanal. Chem., 274 (1989) 167.
9 E. Schmidt, M. Christen and P. Beyeler, J. Electroanal. Chem., 42 (1973) 275.
10 H. Bort, K. Jüttner, W.J. Lorenz and G. Staikov, Electrochim. Acta, 28 (1983) 993.
11 D. Aberdam, C. Salem, R. Durand and R. Faure, Surf. Sci., 239 (1990) 71.
12 B. Parajón Costa, J.C. Canullo, R.C. Salvarezza, D.V. Vásquez Moll, M.C. Giordano and A.J. Arvia, J. Electroanal. Chem., 244 (1988) 261.
13 N. Dimitrov, A. Popov, T. Vitanov and E. Budevski, Electrochim. Acta, 36 (1991) 2077.
14 A. Popov, N. Dimitrov, O. Velev, T. Vitanov and E. Budevski, Electrochim. Acta, 34 (1989) 265.
15 W. Obretenov, U. Schmidt, W.J. Lorenz, G. Staikov, E. Budevski, D. Carnal, U. Müller, H. Siegenthaler and E. Schmidt, J. Electrochem. Soc., 140 (1993) 692.
16 P. Ocón, P. Herrasti, C. Palacio, M.E. Vela, R.C. Salvarezza, L. Vázquez and A.J. Arvia, Electrochim. Acta, in press.

17 P. Carro, A. Hernández Creus, S. González, R.C. Salvarezza and A.J. Arvia, J. Electroanal. Chem., 310 (1991) 361.
18 A. Hernández Creus, P. Carro, S. González, R.C. Salvarezza and A.J. Arvia, J. Electrochem. Soc., 139 (1992) 1064.
19 R.C. Salvarezza and A.J. Arvia, J. Phys. Paris, in press.
20 M. Hansen and K. Anderco, Constitution of Binary Alloys, McGraw-Hill, New York, 1958.
21 A.J. Bard, R. Parsons and J. Jordan (Eds.), Standard Potentials in Aqueous Solution, International Union of Pure and Applied Chemistry, Dekker, New York, 1985.
22 International Critical Tables, Vol II, McGraw-Hill, New York, 1927, p. 421.
23 E. Macchi, Makromol. Chem., 191 (1990) 2217.
24 K. Takayanagi, D.M. Kolb, K. Kambe and G. Lehmpfuhl, Surf. Sci., 100 (1980) 407.
25 T. Vitanov, A. Popov, G. Staikov, E. Budevski, W.J. Lorenz and E. Schmidt, Electrochim. Acta, 31 (1986) 981.
26 P. Herrasti, P. Ocón, L. Vázquez, R.C. Salvarezza, J.M. Vara and A.J. Arvia, Phys. Rev. A, 45 (1992) 7440.
27 J. Gómez, L. Vázquez, A.M. Baró, C. Alonzo, E. González, J. González Velasco and A.J. Arvia, J. Electroanal. Chem., 240 (1988) 77.
28 L. Vázquez, J. Gómez, A.M. Baró, N. García, M.L. Marcos, J. González Velasco, J.M. Vara, A.J. Arvia, J. Presa, A. García and M. Aguilar, J. Am. Chem. Soc., 109 (1987) 1730.
29 W.M. Riggs, L.E. Davis, J.F. Moulder and G.E. Muilenberg in C.D. Wagner (Ed.), Handbook of X-ray Photoelectron Spectroscopy, Perkin-Elmer Corporation, 1978.
30 J. Crank, The Mathematics of Diffusion, Clarendon Press, Oxford, 1975, p. 13.
31 A. Kapoor, R.T. Yang and C. Wong, Catal. Rev. Sci. Eng., 31 (1989) 129.
32 J.M. Blakely, Prog. Mater. Sci., 10 (1963) 395.
33 H.P. Bonzel, in J.M. Blakely (Ed.), Surface Physics of Materials, Academic Press, New York, 1975.
34 N.A. Gojstein, J.J. Burke, N.L. Reed and V. Weiss (Eds.), Surface and Interfaces I, Syracuse University Press, Syracuse, NY, 1967, p. 271.
35 G.E. Rhead, Surf. Sci., 47 (1975) 207.
36 C. Alonso, R.C. Salvarezza, J.M. Vara, A.J. Arvia, L. Vázquez, A. Bartolomé and A.M. Baró, J. Electrochem. Soc., 137 (1990) 261.
37 D. Trevor and C.E.D. Chidsey, J. Vac. Sci. Technol., 9 (1991) 964.
38 C. Alonso, R.C. Salvarezza, J.M. Vara and A.J. Arvia, Electrochim. Acta, 35 (1990) 1331.
39 N. Dimitrov, A. Popov, D. Kashchiev, T. Vitanov and E. Budevski, Electrochim. Acta, 36 (1991) 1259.
40 N. Dimitrov, A. Popov, D. Kashchiev, T. Vitanov and E. Budevski, Electrochim. Acta, 36 (1991) 2077.
41 D. Margheritis, R.C. Salvarezza, M.C. Giordano and A.J. Arvia, J. Electroanal. Chem., 229 (1987) 327.
42 M.W. Breiter, Electrochim. Acta, 34 (1989) 1119.
43 W. Visscher and A.P. Cox, Electrochim. Acta, 37 (1992) 2245.
44 H. Bort, K. Jüttner, W.J. Lorenz, G. Staikov and E. Budevski, Electrochim. Acta, 28 (1983) 985.
45 W.J. Lorenz, L.M. Gassa, V. Schmidt, W. Obretenov, G. Staikov, V. Bostanov and E. Budevski, Electrochim. Acta, 37 (1992) 2173.
46 G. Staikov, E. Budevski, W. Obretenov and W.J. Lorenz, J. Electroanal. Chem., 349 (1993) 355.
47 A.J.E. Welch in W.E. Garner (Ed.), Chemistry of the Solid State, Butterworths, London, 1955, Ch. 12, p. 307.